Compact Diamond X-ray Lens Cubes for Nanofocusing

Wenxin Wang[a,b], Ralph Döhrmann[a], Stephan Botta[a], Ayush Sharma[a], Anders Madsen[b], Christian G. Schroer[a,c,d], and Frank Seiboth[a]

[a]Center for X-ray and Nano Science CXNS, Deutsches Elektronen-Synchrotron DESY, Notkestr. 85, 22607 Hamburg, Germany
[b]European X-Ray Free-Electron Laser Facility, Holzkoppel 4, 22869 Schenefeld, Germany
[c]Department Physik, Universität Hamburg, Luruper Chaussee 149, 22761 Hamburg, Germany
[d]Helmholtz Imaging, Deutsches Elektronen-Synchrotron DESY, Notkestr. 85, 22607 Hamburg, Germany

ABSTRACT

Nanofocusing with refractive X-ray optics requires the combination of many single lenses into a larger lens stack to achieve high numerical apertures. So far, these optics have suffered from aberration due to accuracy limitations in X-ray lens manufacturing. Refractive phase plates have been used to compensate these errors, but require separate alignment and wavefront metrology. Here, we present the concept of X-ray lens cubes, a new assembly strategy developed for laser-ablated diamond X-ray lenses. It allows to integrate a diamond phase corrector directly into the quasi-monolithic assembly, creating lens cubes that contain several lenses with a matching and pre-aligned phase corrector. We show the experimental validation of individual lens cubes, as well as the stacking of two cubes to form a larger lens stack. The concept and advantages of integrating multiple phase plates into a lens assembly are validated by numerical simulations. Aberration-compensated lens cubes can offer near diffraction-limited imaging performance over a broad X-ray energy range in combination with easy alignment, providing broad practical applicability for nano-imaging experiments in the hard X-ray regime.

Keywords: X-ray optics, diamond lenses, aberration correction, laser ablation, ptychography

1. INTRODUCTION

Diamond X-ray lenses have emerged as a promising alternative to aluminum and beryllium compound refractive lenses (CRLs) for focusing hard X-ray beams at synchrotron radiation and X-ray free-electron laser facilities. Their fabrication is based on laser ablation of diamond in order to create a concave lens profile into a diamond substrate. As either chemical vapor deposition (CVD) or high pressure high temperature (HPHT) single-crystal substrates with high purity are used, the optical quality of fabricated lenses mainly depends on the accuracy of the milling process via laser ablation. A steady development in laser ablation technology has led to tremendous improvements in their shape accuracy in recent years.[1–3] However, the lenses still exhibit significant shape inaccuracies in the order of a few micrometer, effectively preventing diffraction-limited focusing for high numerical apertures (NA), where several of these lenses are combined. In addition, past developments were relying on the stacking of individual lens elements, either small diamond cylinders[1] and plates,[2] or diamonds pressed into a round casing.[3] So far, none of these approaches could offer the accuracy, repeatability, and ease of handling in a combined package in order to reliably configure a larger stack of diamond lenses with a fixed aberration signature. Especially due to the rotational symmetric nature of the widely used 12 mm round lens coins[3,4] an easy and repeatable alignment was not trivial. Achieving this reliability is a key element in order to compensate eventual fabrication errors in the lenses by means of a static refractive phase corrector,[5,6] as changes in the lens stacking can alter the induced aberrations. While aberration compensation by these phase correctors is nowadays routinely used in imaging applications,[7–12] their alignment often requires at-wavelength metrology and expert knowledge.

Further author information: (Send correspondence to F.S.)
F.S.: E-mail: frank.seiboth@desy.de

Here, we present diamond X-ray lens cubes (LC) for the assembly of a hard X-ray lens made out of single-crystal diamond substrates. The mechanical stability of diamond in combination with a precise substrate shape and micrometer-level positioning accuracy enable the assembly of a quasi-monolithic X-ray lens comprising of multiple lens elements in combination with a pre-aligned and tailored aberration-compensating phase plate made out of diamond.[13] The LC not only pre-aligns the lenses and phase corrector into a single optical element, but also reduces the inter-lens distance to a minimum, allowing for the direct stacking of diamond substrates back-to-back with no air gap. Venting channels for in-vacuum use can be integrated directly into the diamond substrates. In this study, we show the experimental validation of the LC concept and also demonstrate the advantages of minimizing the inter-lens distance as well as the use of multiple phase plates within the lens assembly by numerical simulations. These advancements can offer near diffraction-limited hard X-ray imaging capabilities for the non-expert user with a broad applicability at both synchrotron radiation and X-ray free-electron laser facilities.

2. LENS CUBE FABRICATION

Diamond lens plates used in this study were single-crystal CVD diamond plates in mechanical grade with lateral dimensions of 3 mm × 3 mm and a thickness of 0.5 mm. Both sides of the substrates were polished to a surface roughness of 30 nm. They were processed via ultra-short pulsed laser ablation[14] using an Amplitude Satsuma HP^2 ytterbium-doped fiber laser with a fundamental laser wavelength of 1032 nm and a pulse duration of 285 fs. The laser was operated with a third-harmonic frequency-conversion unit at a wavelength of 343 nm and a pulse energy of up to 3 µJ at a repetition rate of 1 MHz. The pulse energy was adjusted to achieve a uniform material removal and minimal surface roughness. Individual pulses were triggered position based from the encoder position of the stages. For lateral displacement of the sample a planar XY scanner with air bearing was used. Height translation of the laser focus was achieved by moving the focusing objective with a linear air bearing stage. Laser pulses were focused on the surface of the substrate by an objective with NA 0.36, resulting in a spot size below 1 µm. The lens shape was created by subsequently removing material layer by layer. First, a parabolic lens volume was removed from one side of the diamond substrate. Subsequently, an identical paraboloid was removed on the opposite side to form a bi-concave lens of two aligned and opposed paraboloid structures. The targeted radius of curvature R of the lens was 50 µm, while the geometrical aperture D can reach up to 312 µm. We aimed for a distance d between the two lens vertices of 10 µm to minimize absorption.

For in-lab metrology a Keyence VK-X1100 confocal laser scanning microscope (LSM) with a 50× objective and $NA = 0.95$ was used. The LSM provides a means of quality control and was used to refine ablation parameters as well as the paraboloid shape. An example of such a shape measurement is shown in Fig. 1a). The map shows 2D measurement data after the removal of a fitted paraboloid of rotation with a curvature of $R = 50.0\,\mu\text{m}$. The fit reveals concentric rings on the lens surface with an amplitude of 0.5 µm as well as some non-rotational symmetric surface errors. A radially-averaged error profile is shown in Fig. 1b), highlighting the fabrication reproducibility, especially for the mentioned ring features for radii below 100 µm.

After fabricating 20 lens plates, 10 each were combined into a LC. The LC consists of a mechanical assembly unit, comprising an alignment prism (blue prism shown in Fig. 1c), two springs (red part in Fig. 1c), and a holding clamp (orange part in Fig. 1c). After compressing the springs, the holding clamp is slid over the assembly and is held in place by friction.

3. EXPERIMENTAL CHARACTERIZATION AND PHASE PLATE INTEGRATION

In this study, a total of 20 lenses were manufactured, and each set of 10 lenses was initially assembled into a LC. To design and fabricate the phase plates[15] capable of correcting the aberrations introduced by each set of lenses, the focused wavefield of each LC was characterized by at-wavelength metrology based on X-ray ptychography,[16,17] offering the possibility of reconstructing the complex wavefield of the X-ray beam. The ptychographic imaging experiments were conducted at the microprobe endstation of beamline P06 of PETRA III at DESY. A photon energy of $E_0 = 15\,\text{keV}$ was selected by a Si(111) monochromator. The schematic configuration of the experiment can be seen in Fig. 2. An entrance aperture pinhole with $A = 300\,\mu\text{m}$ diameter (Pt/Ir (95/5%) for electron-microscopy use, PLANO GmbH) was placed roughly 5 mm upstream of LC to confine the illuminating X-ray beam. The pinhole diameter A is intentionally designed to be slightly smaller than the lens aperture in order

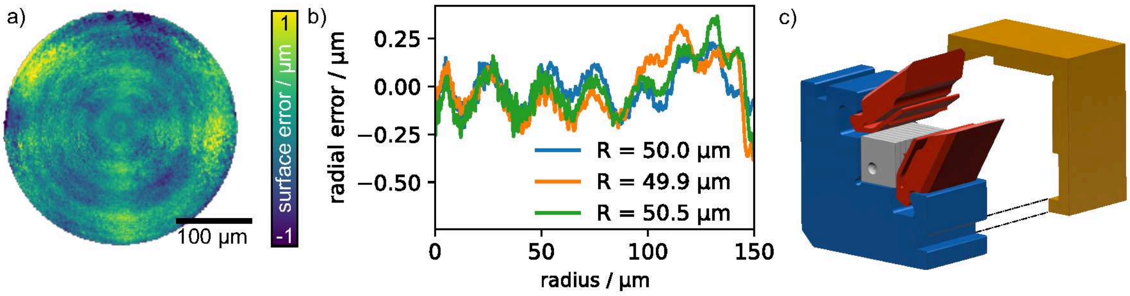

Figure 1. Single diamond lens surface and its shape error measured by the LSM. a) 2D height error map (0.637 μm RMSE) of the single diamond lens surface with respect to a paraboloid fit with $R = 50.0\,\mu\mathrm{m}$. The measured geometric aperture is 314 μm. b) Radially averaged error profile of three different lens surfaces as an example for fabrication repeatability. The blue line represents the lens in a), while the others have fitted R of 49.9 μm and 50.5 μm, respectively.

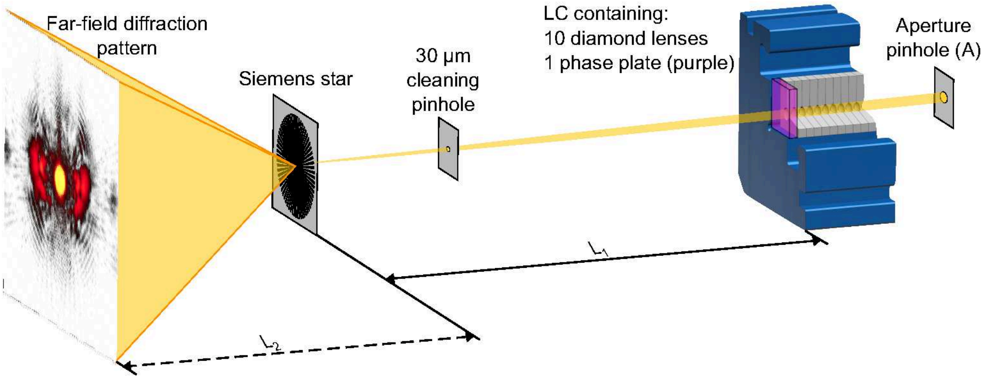

Figure 2. Schematic of the ptychography experiment setup at beamline P06 of PETRA III. For the pre-characterization, 2 sets of LCs with 10 diamond lenses each at 15 keV were used. Subsequently, a phase plate (purple plate) was added to each of the LC, whose design is based on the previous measurements.

to restrict the X-ray beam size and ensure that the beam passes through the lenses without scattering from the edges. X-rays were focused by $N = 10$ diamond lenses with $R = 50\,\mu\mathrm{m}$, yielding a total lens thickness of roughly 5 mm and a theoretical focal length $f = 769\,\mathrm{mm}$ at E_0. A 30 μm diameter cleaning pinhole was placed between the diamond lenses and the test sample close to the focal plane to reduce scattering. A Siemens star resolution test object made of 500 nm thick tantalum with 50 nm smallest features (NTT-AT XRESO-50HC)was placed in the vicinity of the focal plane. The object was scanned in a grid with 500 nm step size, covering an area of $5\,\mu\mathrm{m} \times 5\,\mu\mathrm{m}$ in 10×10 steps with a dwell time of 0.5 s per scan point. In order to increase the lateral coherence length in horizontal direction, high-power front end slits, located roughly 27 m downstream from the X-ray source, were closed to 30 μm horizontally. A Dectris EIGER X 4M pixel detector[18] was used to record far-field diffraction patterns at a distance of 8376 mm downstream of the sample. Experimental parameters, distances and also measurement results are summarized in Table 1. The pre-characterizaton results are denominated by a 'no' in the 'phase plate' column.

Initially, the two assembled LC were characterized individually. The complex wavefield for each LC at the object plane was obtained via ptychographic phase retrieval. By numerically propagating the complex wavefield using the Fresnel-Kirchhoff diffraction formula by 774 mm from the object plane to the exit of the lens stack along the optical axis, the wavefield at the exit plane of each LC was retrieved. The corresponding wavefront error was then obtained by fitting the first 6 Zernike polynomials for a circular aperture to correct for tilt, defocus and astigmatism, as depicted in Fig. 3a) and 3b). The wavefront error maps indicate that both LCs exhibit a comparable shape error that is closely distributed in a rotationally symmetric manner. This demonstrates both the repeatability of the lens fabrication as well as the lens stacking within the LC, but also shows that individual characterization of each stack is still required. The obtained wavefront error clearly shows concentric ring-shaped phase errors that somewhat resemble the measured surface error profile from the LSM, as shown in

Table 1. Parameters of the characterization experiment for the two LCs at 15 keV and the combined LCs at 12, 15 and 20 keV. A is the aperture of the entrance pinhole (cf. Fig. 2).

E (keV)	No. of lenses N	A (µm)	Phase plate	L_1 (mm)	L_2 (mm)	Spot size (HxV, nm^2)	Wavefield RMSE (rad)	Strehl ratio
15	10	300	no	774	8376	257×275	0.862	0.54
			yes			249×245	0.273	0.83
15	10	300	no	774	8376	252×252	0.693	0.63
			yes			263×250	0.386	0.80
12	20	300	yes	247.1	8376	152×155	0.585	0.73
15	20	300	no	386.2	8376	163×127	1.197	0.32
			yes			187×188	0.506	0.78
20	20	300	yes	689.4	8376	197×191	0.412	0.76

Fig. 1, indicating that the offline metrology is capable to reveal manufacturing errors on a relevant scale for this lens geometry. The radially-averaged wavefront error profile is depicted in Fig. 3e) by the solid lines for both LC. Subsequently, the retrieved phase error φ_ϵ at the LC exit is converted into a shape error z_ϵ by

$$z_\epsilon = \frac{\varphi_\epsilon}{-k\delta_{\mathrm{C}^*}(E)}, \qquad k = \frac{E}{\hbar c}, \tag{1}$$

where $\delta_{\mathrm{C}^*}(E)$ is the refractive index decrement of diamond at photon energy E, k is the wavenumber, $\hbar$ is the reduced Planck constant, and c is the speed of light in vacuum. These values are indicated by the secondary color bar in Fig. 3.

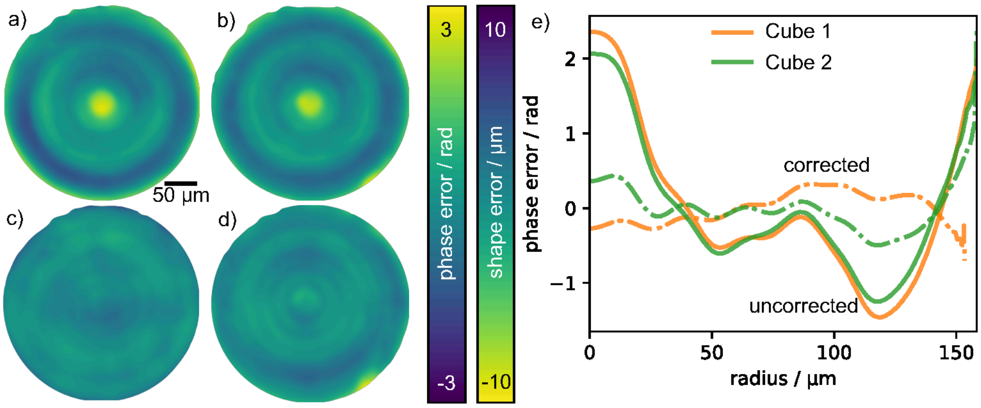

Figure 3. Residual wavefield error in the plane of the LC exit at 15 keV with $N = 10$ lenses. a) and b) Wavefield error of LC1 (0.862 rad RMSE) and LC2 (0.693 rad RMSE) without phase plate in each cube. c) and d) Wavefield error of LC1 (0.273 rad RMSE) and LC2 (0.386 rad RMSE) with phase plate in each cube. The scale bar in a) is shared among others. e) Radially averaged wavefront error profiles.

The phase plate structure was determined by directly converting the non-radially symmetric two-dimensional height error maps shown in Fig. 3a) and 3b) into a height-based shape map with an offset to avoid negative values. These structures were implemented on two separate diamond substrates with a thickness of only 0.25 mm and identical lateral dimensions of 3 mm × 3 mm. The thinner substrates were chosen in order to minimize time to further thin down the substrates by laser ablation for optimized X-ray transmission. Here, the substrates were thinned to a thickness of 50 µm locally at the phase plate location. Afterwards, the phase plate structures were ablated. The maximum height difference for these phase plates is 18.5 µm and 14 µm for LC1 and LC2, respectively. In this way, two individual phase plates were fabricated for each corresponding stack of 10 lenses. The phase plates were added to the two LC by opening the clamping assembly, adding the additional diamond substrate to each LC, and closing the cube again with the springs and holding clamp.

After re-assembly, each stack was measured individually again under the same conditions as described above. The phase plate manufacturing was performed over night and the corrected LCs could be used on the next day at the beamline. The obtained wavefront errors for the two LCs are depicted in Fig. 3c) and 3d), respectively, showing a strong improvement for the wavefront error, especially for the pronounced central feature, but also for the outer rings. However, higher-frequency ring features could not be removed completely, as can be seen in the maps and also in the radially-average dash-dotted line plots in Fig. 3e).

Next, the stacking capability of the LCs should be demonstrated in order to confirm the possibility to assemble larger lens stacks out of individual LCs. By combining LC1 and LC2, we created a lens stack with $N = 20$ lenses with two integrated phase plates after each 10 lenses. Fig. 4a) shows the wavefront error of both LCs combined before integrating the phase plates at E_0 and Fig. 4b) the error on the next day after phase plate integration. Again, the large central feature and outer rings could be corrected, the higher-frequency ring structure persist. The data is presented radially averaged in Fig. 4c), where the successful correction of the central feature and the two outer ring features is more clearly visible. For this configuration a transmission of 38 % in good agreement with theoretical values was measured at E_0. The wavefront characterization with installed phase plates was also repeated at a photon energy of 12 keV and 20 keV. These results are only shown in Fig. 4c) and the obtained beam parameters are summarized in Table 1 as well. Although the energy was changed dramatically, the aberration compensation worked on a comparable level for all three X-ray energies. By dividing the full lens stack into two smaller stacks with a phase plate for each, one can increase the working energy range for refractive phase plates. Since each sub stack is thinner than the complete lens stack, propagation effects in these thick optical elements are less relevant. Numerical simulations to show this concept are presented later in Section 4.

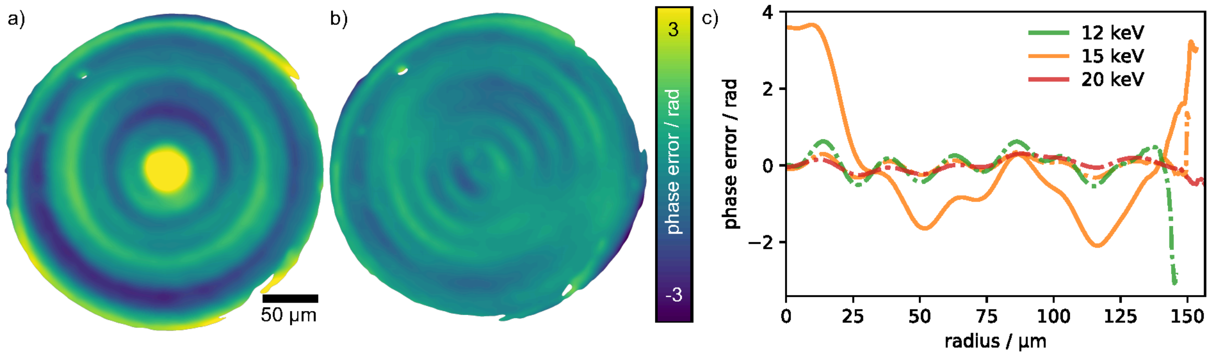

Figure 4. Comparison of the wavefront error for the combined LCs with $N = 10 + 10 = 20$ lenses in total. a) Wavefront error (1.197 rad RMSE) at the exit of the LCs without phase plates at 15 keV. b) Wavefront error (0.506 rad RMSE) at the exit of the LCs with phase plates at 15 keV. c) Radially averaged wavefront error at different photon energies. The solid line shows the error profile without phase plates, the dash-dotted lines with installed phase plates.

By numerically propagating the retrieved wavefield from the sample plane along the beam axis, a beam caustic can be obtained. The horizontal beam caustic before correction is presented in Fig. 5a) and with phase plates installed in Fig. 5c), respectively. The uncorrected beam caustic shows strong intensity on the optical axis before and after the focal plane, indicating the spherical aberration induced by the rotational-symmetric ring-shaped surface errors on the fabricated diamond lenses. A strong improvement is visible with the installed phase plates, removing almost all spherical aberration, although some asymmetric features are still visible. This is also highlighted by the focal spot intensity, presented in Figs. 5b) and 5d) for the uncorrected and corrected LC assembly, respectively. While the uncorrected focus shows distinct asymmetric side lobes and a weak outer ring, these features almost vanish for the corrected beam, that only exhibits some weak tails in a four-fold symmetry. In all investigated cases the wavefront RMSE and Strehl ratio could be improved significantly, summarized in Table 1.

4. NUMERICAL MODELLING

In order to understand the influence of inter-lens distance, phase plate placement, and number of phase plates for the focusing performance of optically thick lens stacks, numerical simulations were carried out. The presented cases and lens properties follow closely the results from Section 3. The investigated scenarios together with the used lens deformation are given in Fig. 6 as an overview. Fig. 6a) shows the typical scenario for a CRL. Due to

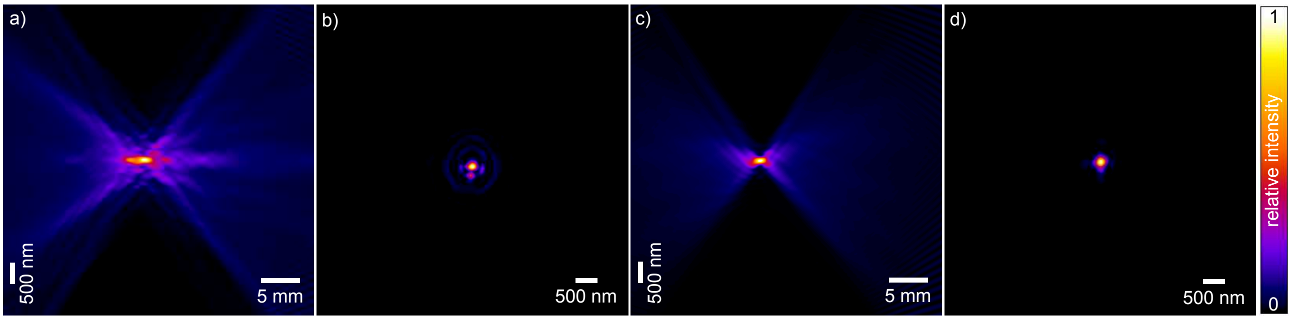

Figure 5. Beam and focus quality of the combined LCs, containing $N = 10 + 10 = 20$ diamond lenses, without and with phase plate at 15 keV. a) Horizontal beam caustic without phase plates. b) Focal spot intensity without phase plates. c) Horizontal beam caustic with phase plates. d) Focal spot intensity with phase plates.

the lens casing for each single lens, the inter-lens distance is large, in this case 2 mm. When the X-ray energy is changed, the refractive power of each lens element is altered, leading to a different beam convergence trajectory within the optically thick lens stack and consequently to a change in focal length. The solid yellow beam represents the beam at the set design X-ray energy E_0, where the downstream-mounted phase plate matches very well to the beam and its aberration pattern. The higher energy scenario is indicated by the dashed line, the lower energy case by the dotted line. It can be seen that the phase plate size will not fit for these non-default energies, as the beam size at the fixed phase plate position changes with X-ray energy. In the following simulations the phase plate position was kept constant. However, one could also move the phase plate along the optical axis to compensate for a change in beam size.[19] While this will definitely improve the phase plate fit, changes in the aberration pattern due to the different beam trajectory in the lens stack can not be accounted for. In addition, the phase plate can typically not be moved by arbitrary distances upstream, which is required at lower X-ray energies, as it will inevitably collide with the lens stack itself at some point. The issue can be partially avoided if the initial phase plate design position is further downstream from the lens exit. Furthermore, re-alignment of the phase plate is typically required after moving it along the optical axis.

An alternative approach is shown in Fig. 6b), where the phase plate is positioned upstream at the lens entrance. This placement avoids the problem of varying beam sizes encountered downstream from the lens and potential repositioning along the optical axis. However, the phase plate shape will only be optimal for the design energy E_0, as the aberration pattern will change with a different beam trajectory through the lens stack for $E \neq E_0$, as mentioned before. While the measurement of beam aberrations downstream of the lens stack is straight forward and the results can directly be used to design the phase plate, as described earlier in Section 3, the design of an upstream-mounted phase plate is more complicated. It requires knowledge of every single lens element, their positioning with respect to each other, and an iterative refinement process to find the optimal phase plate shape. In the presented simulations the knowledge about every single lens element is trivial and a Gerchberg-Saxton (GS) algorithm[20] was used to find the phase plate shape.

By directly stacking the lens substrates back-to-back, as realized within the presented LC, the inter-lens distance is minimized, here to 0.5 mm. This scenario is illustrated in Fig. 6c). Especially for nano-focusing applications, where the focal length is typically short and many lenses are required to achieve a sufficient NA, this approach will reduce the required lens stack thickness by more than a factor of 4, compared to CRLs with 2 mm inter-lens distance. This significant reduction in optical thickness leads to a reduction in beam trajectory differences within the lens stack for a given X-ray energy range. With the LC concept the optical thickness can be further reduced by the introduction of multiple phase plates within the lens stack, illustrated in Fig. 6d). Here, each phase plate effectively only corrects induced aberration from a sub stack of the lens system. By choosing the number of lenses per phase plate, taking measurements and manufacturing limitations for the phase plate shape into account, an optimized number of phase plates can be found. This optimization also depends on the particular aberration pattern of the lenses themselves. If the lenses themselves have almost no aberration, it is plausible that less phase plates are required and a phase plate can be employed for a larger lens stack without tremendous negative impact of the aberration correction over a given X-ray energy range.

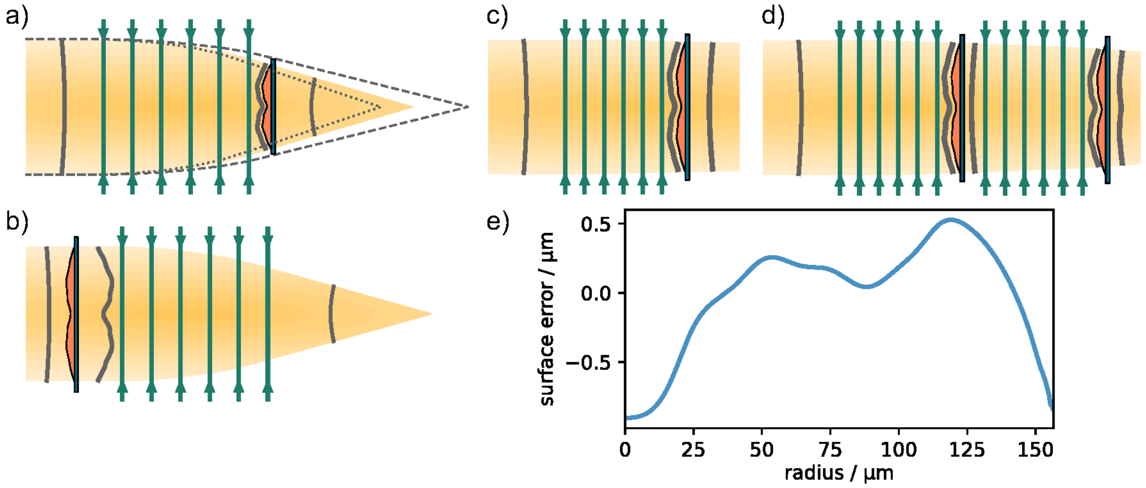

Figure 6. Schematics of wavefield propagation through thick lens stacks with different inter-lens distances and phase plate configurations. a) Illustration of a lens stack with large inter-lens distance and the phase plate located downstream of the lens stack. The orange-colored area represents the X-ray beam at the design energy for the phase plate. The dashed line represents the beam at a higher X-ray energy and the dotted line shows the beam at a lower X-ray energy, highlighting the potential issues regarding phase plate fit at X-ray energies different than the design photon energy. b) Upstream-mounted phase plate in combination with a lens stack with large inter-lens distances. c) Lens stack with short inter-lens distances and downstream-mounted phase plates. d) Illustration of slicing a lens stack into multiple thinner sub stacks, here two, with corresponding phase plates for each sub stack. e) Bi-concave lens error profile for a lens with $R = 50\,\mu\mathrm{m}$ used in subsequent simulations. The profile is adapted from the measured phase error profiles shown in Fig. 3.

Numerical calculations were performed on the DESY Maxwell HPC Cluster on a single Nvidia A100 with 80 GB memory. For simulations we used a field size of 16 384 px × 16 384 px with a pixel size of 20 nm, yielding a field of view of 327.68 µm × 327.68 µm. These parameters were chosen to cover the full lens aperture of 300 µm and achieve a sufficient sampling of the phase gradient for these nano-focusing optics with high NA. For propagation we used the Fresnel-Kirchhoff diffraction integral implemented in Python using CuPy. The propagation operator $(\mathcal{K}_{\Delta z}\bullet)(x,y)$ for a distance Δz along to optical axis is given by

$$(\mathcal{K}_{\Delta z}\bullet)(x,y) = \mathcal{F}^{-1}\{\mathcal{F}\{\bullet\}\mathcal{F}\{K_{\Delta z}\}\} \tag{2}$$

with $(\mathcal{F}\bullet)$ being the Fourier transform operator and the propagator Kernel K is defined as

$$K_{\Delta z}(x,y) = -\frac{\mathrm{i}k}{4\pi}\frac{e^{\mathrm{i}k\Delta z}}{\Delta z}e^{\frac{\mathrm{i}k}{2\Delta z}(x^2+y^2)}\ . \tag{3}$$

The wave field $\psi_0(x,y)$ was initialized with a flat amplitude and phase as a plane wave. The complex transmission operator of a lens element $(\mathcal{T}_{\mathrm{lens}}\bullet)(x,y)$ is given by

$$(\mathcal{T}_{\mathrm{lens}}\bullet)(x,y) = \bullet(x,y)\cdot e^{\mathrm{i}knd_{\mathrm{lens}}(x,y)}\ . \tag{4}$$

Here, n is the complex refractive index of the lens material and $d_{\mathrm{lens}}(x,y)$ is the parabolic thickness profile of the lens with the radial symmetric surface error applied, as shown in Fig. 6e). Propagation through a lens stack with N lenses and an inter-lens distance Δz can be described as

$$\psi_{\mathrm{exit}} = [\mathcal{T}_{\mathrm{lens}}\mathcal{K}_{\Delta z}]^{N-1}\mathcal{T}_{\mathrm{lens}}\psi_0\ . \tag{5}$$

The obtained exit wavefield ψ_{exit} is subsequently fitted to the first 6 Zernike polynomials for a circular aperture. This data is then used to calculate the phase plate shape $d_{\mathrm{dsPP}}(x,y)$ for the downstream-mounted case[21] at the design X-ray energy of $E_0 = 15\,\mathrm{keV}$. In the case of multiple phase plates within the $N = 20$ lens stack, the initial phase plate calculation is carried out for a stack of $N = 10$ once, and the resulting phase plate shape $d_{\mathrm{dsPP10}}(x,y)$ is used repeatedly, in this example with $N = 20$ exactly twice, within the larger lens stack.

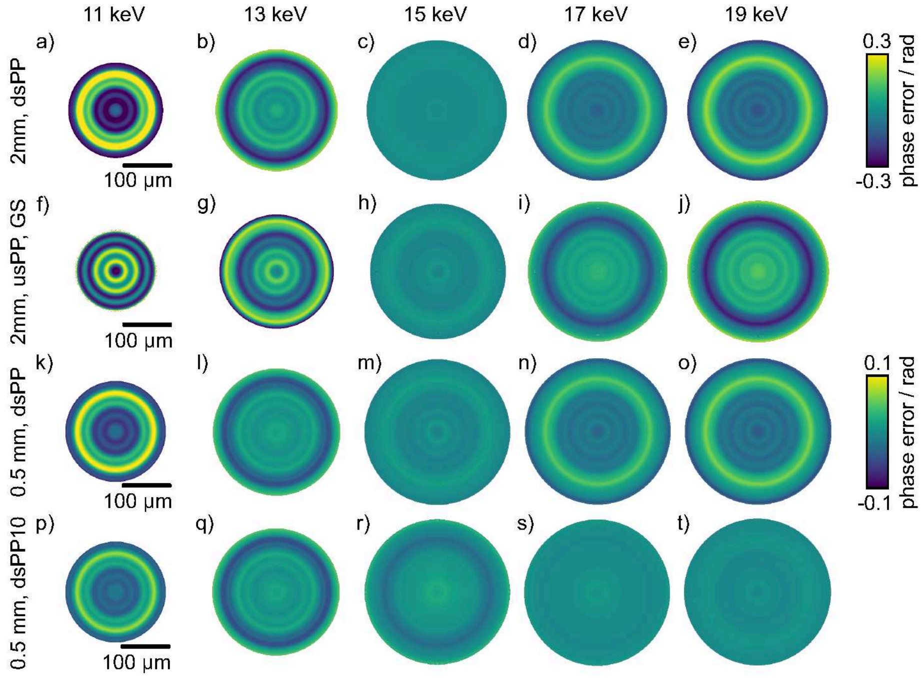

Figure 7. Simulated wavefields at the exit of the lens stack for various configurations (marked on the left) and X-ray energies (marked at the top). All lens stacks contain $N = 20$ lenses with $R = 50\,\mu\text{m}$ and $A = 300\,\mu\text{m}$. The phase plates have been optimized for an X-ray energy of $E_0 = 15\,\text{keV}$. a) - e) Wavefields at the lens exit for a stack with 2 mm inter-lens distance and downstream-mounted phase plate (dsPP). f) - j) Wavefields at the lens exit for a stack with 2 mm inter-lens distance and upstream-mounted phase plate that was optimized via a Gerchberg-Saxton algorithm (usPP, GS). k) - o) Wavefield at the lens exit for a stack with 0.5 mm inter-lens distance and downstream mounted phase plate. p) - t) Wavefields at the lens exit for a stack with 0.5 mm inter-lens distance and two downstream-mounted phase plates after every 10 lenses (dsPP10). The upper color bar belongs to a) - e), while the lower color bar belongs to f) - t). All sub figures share the same scale bar.

For the upstream-mounted case the phase plate transmission operator $\mathcal{T}_{\text{usPP}}$ is unknown at first. For a perfect lens with the shape of a paraboloid of revolution and the transmission operator $\mathcal{T}_{\text{paraboloid}}$, the expected exit wavefield $\psi_{\text{exit, perfect}}$ is given by

$$\psi_{\text{exit, perfect}} = [\mathcal{T}_{\text{paraboloid}}\mathcal{K}_{\Delta z}]^{N-1}\mathcal{T}_{\text{paraboloid}}\psi_0 \ . \tag{6}$$

The upstream-mounted scenario is described by

$$\psi_{\text{exit, usPP}} = [\mathcal{T}_{\text{lens}}\mathcal{K}_{\Delta z}]^{N-1}\mathcal{T}_{\text{lens}}\mathcal{T}_{\text{usPP}}\psi_0 \ . \tag{7}$$

Note that potential propagation operators between phase plate and lens are omitted here, but can easily be implemented. In order to determine T_{usPP}, we need to solve the inverse problem

$$(T_{\text{usPP}}) = \arg\min ||\psi_{\text{exit, usPP}} - \psi_{\text{exit, perfect}}|| \ . \tag{8}$$

Here, we chose a simple iterative approach based on the GS algorithm.[22] In the upstream-mounted phase plate plane $\psi_{\text{usPP}} = \mathcal{T}_{\text{usPP}}\psi_0$ we are enforcing the amplitude of the incoming beam $|\psi_0|$, but let the phase free to evolve. For the second plane at the lens exit we enforce the phase of the perfect lens system $\arg(\psi_{\text{exit, perfect}})$ and let the amplitude evolve freely. In a first step, the initial wavefield ψ_0 is multiplied with an empty phase plate transmission and propagated through the aberrated lens stack to obtain $\psi_{\text{exit, usPP}}$. In step two, the phases in that plane are replaced with the ones from the perfect lens system $\arg(\psi_{\text{exit, perfect}})$. Third, the wavefield is back-propagated through the aberrated lens stack to the plane of the phase plate ψ_{usPP}. Lastly, the amplitudes of the wavefield are replaced by that of the inital one $|\psi_0|$. This cycle is repeated until convergence. Since the

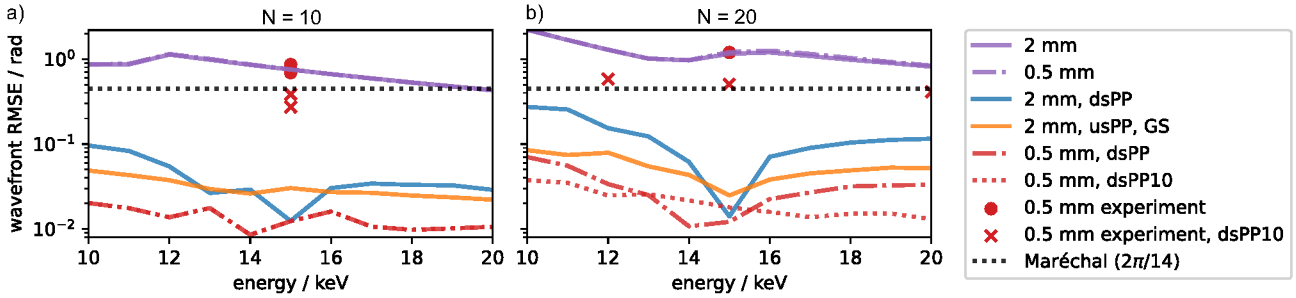

Figure 8. Behaviour of the wavefront RMSE for different lens and phase plate configurations between 10 keV to 20 keV for phase plates optimized at 15 keV. The purple lines show the wavefront error without phase plates for an inter-lens distance of 2 mm (solid) and 0.5 mm (dash-dotted), respectively. The red circles and red crosses mark experimental results shown previously in Figs. 3 - 5 without and with installed phase plates, respectively. a) Wavefront RMSE for a stack of $N = 10$ lenses. b) Wavefront RMSE for a stack of $N = 20$ lenses. The horizontal black-dotted lines marks the Maréchal criterion in order for a lens to be considered diffraction limited. The used abbreviations have the following meaning: dsPP = single downstream-mounted phase plate, usPP = single upstream-mounted phase plate, GS = Gerchberg-Saxton optimized, dsPP10 = downstream mounted phase plates for every 10 lenses.

phase plate is made from a single material, the height profile $d_{\mathrm{usPP}}(x, y)$ can be calculated from the retrieved phase shift.

In all further simulation studies the obtained phase plate height profiles were kept constant, but the X-ray energy E was varied between 10 keV to 20 keV in 1 keV steps. After propagating the wavefield through all optical elements, the final exit wavefield ψ_{exit} is again fitted to the first 6 Zernike polynomials for a circular aperture in order to retrieve the wavefront error. A selection of the retrieved wavefields is shown in Fig. 7. From these 2D error maps the obtained root mean square error (RMSE) is plotted in Fig. 8 for all energies and configurations. The measured experimental results are indicated by a red circle for the LC without any phase plates and by red crosses for the LC with equipped phase plates. In the case of no installed phase plates, the results agree very well to the simulation, indicated by the purple lines. Although the beam is converging significantly inside the lens stack, there is almost no visible difference in the wavefield RMSE for the two different inter-lens distances of 2 mm and 0.5 mm, marked by the solid and dash-dotted purple lines in Fig. 8, respectively. The simulation results for lenses with equipped phase plates show much lower wavefront RMSE as in the experiment. This is to be expected as the simulated phase plates match almost perfectly and do not suffer from any manufacturing or positioning inaccuracies. A general observation across all configurations between Fig.8a) for $N = 10$ and Fig. 8b) for $N = 20$ lenses is that the wavefront RMSE increases stronger when deviating from the design X-ray energy E_0 with more lenses in the stack, independent from the chosen phase plate configuration. For the lens stack with 2 mm inter-lens distance (coin-shaped CRL), two possible configurations were investigated. The solid blue line shows the results for the downstream-mounted phase plate with significant increases in wavefront RMSE when deviating from E_0. The upstream-mounted configuration on the other hand, marked by the solid orange line, shows much less increase in wavefront RMSE, but at E_0 the correction of aberration is not as good, since the iterative algorithm was not able to converge to a better solution. In general, the corrected LC with an inter-lens distance of only 0.5 mm performs better than the coin-shaped CRL with $\Delta z = 2.0$ mm. This is due to the mentioned reduction in optical thickness and therefore a reduced sensitivity to changes in the beam path trajectory with the LC, as illustrated before in Fig. 6. For $N = 10$ lenses, shown in Fig. 8a), there is no difference between the LC with dsPP and dsPP10, marked by the dash-dotted and dotted red lines, respectively. Both cases employ only a single phase plate for each 10 lenses. However, when looking at the $N = 20$ scenario in Fig. 8b), there is a strong difference between the two. When using a phase plate for each 10 lenses (dsPP10, dotted red line), a slower increase with deviating X-ray energy from E_0 is observed, although the error closely around E_0 is higher as for the case with only a single phase plate for the full $N = 20$ stack (dsPP, dash-dotted red line). Since for the dsPP10 case both phase plates were optimized for a $N = 10$ stack, when combining two of these into a stack with $N = 20$ their fit is not as good as for a single phase plate. But distributing multiple phase plates across the stack leads to a more uniform wavefront error across a wide X-ray energy range, which is often more beneficial than a perfect fit at a single energy. For real world applications one also needs to consider that the phase plates will never fit that well in the first place. A slow increase in wavefront error seems therefore more beneficial, as has been demonstrated experimentally for a larger LC assembly with up to 60 lenses.[13]

5. CONCLUSIONS

Aberration correction using phase plates has become routine in recent years for nano-focusing applications.[7–12] However, until recently[13] the phase plate was always added externally, requiring careful alignment and wavefront metrology.[15] Here, we presented the concept of compact lens cubes (LCs) for diamond refractive X-ray lenses that integrate the corrective phase plate, also made out of diamond, directly into the lens stack. This approach enables the fabrication of a quasi-monolithic X-ray lens with high numerical aperture and integrated aberration compensation. The individual LCs can be freely combined, and each LC can host one or even multiple phase plates.

This new lens assembly concept provides a broad practical applicability for nano-imaging experiments that rely on refractive optics for their compactness, ease of use, and inline geometry. The LC is used in practice like coin-shaped CRLs, following the same alignment routines and offering a compatibility to existing CRL mounts. No further wavefront metrology is required to achieve a close to diffraction-limited performance, which is especially useful in time-critical experiments or complicated multi-lens setups, e.g. for simultaneous bright- and dark-field imaging at X-ray free-electron laser sources.

ACKNOWLEDGMENTS

Parts of this research were carried out at beamline P06 of PETRA III at Deutsches Elektronen-Synchrotron DESY, a member of the Helmholtz Association (HGF). This research was supported in part through the Maxwell computational resources operated at Deutsches Elektronen-Synchrotron DESY. The authors are grateful for beamline support at P06 from Gerald Falkenberg, Dennis Brückner, Ken Vidar Falch, and Jan Garrevoet.

REFERENCES

[1] Terentyev, S., Blank, V., Polyakov, S., Zholudev, S., Snigirev, A., Polikarpov, M., Kolodziej, T., Qian, J., Zhou, H., and Shvyd'ko, Y., "Parabolic single-crystal diamond lenses for coherent x-ray imaging," *Applied Physics Letters* **107**(11), 111108 (2015).

[2] Terentyev, S., Polikarpov, M., Snigireva, I., Di Michiel, M., Zholudev, S., Yunkin, V., Kuznetsov, S., Blank, V., and Snigirev, A., "Linear parabolic single-crystal diamond refractive lenses for synchrotron x-ray sources," *Journal of Synchrotron Radiation* **24**, 103–109 (Jan 2017).

[3] Celestre, R., Antipov, S., Gomez, E., Zinn, T., Barrett, R., and Roth, T., "Polished diamond x-ray lenses," *Journal of Synchrotron Radiation* **29** (mar 2022).

[4] Lengeler, B., Schroer, C. G., Benner, B., Gunzler, T. F., Kuhlmann, M., Tummler, J., Simionovici, A. S., Drakopoulos, M., Snigirev, A., and Snigireva, I., "Parabolic refractive x-ray lenses: a breakthrough in x-ray optics," *Nuclear Instruments and Methods in Physics Research Section A: Accelerators, Spectrometers, Detectors and Associated Equipment* **467**, 944–950 (2001).

[5] Sawhney, K., Laundy, D., Dhamgaye, V., and Pape, I., "Compensation of x-ray mirror shape-errors using refractive optics," *Applied Physics Letters* **109**(5), 051904 (2016).

[6] Seiboth, F., Schropp, A., Scholz, M., Wittwer, F., Rödel, C., Wünsche, M., Ullsperger, T., Nolte, S., Rahomäki, J., Parfeniukas, K., Giakoumidis, S., Vogt, U., Wagner, U., Rau, C., Boesenberg, U., Garrevoet, J., Falkenberg, G., Galtier, E. C., Lee, H. J., Nagler, B., and Schroer, C. G., "Perfect x-ray focusing via fitting corrective glasses to aberrated optics," *Nature Communications* **8**, 14623 (Mar. 2017).

[7] Vassholz, M., Hoeppe, H. P., Hagemann, J., Rosselló, J. M., Osterhoff, M., Mettin, R., Kurz, T., Schropp, A., Seiboth, F., Schroer, C. G., Scholz, M., Müller, J., Hallmann, J., Boesenberg, U., Kim, C., Zozulya, A., Lu, W., Shayduk, R., Schaffer, R., Madsen, A., and Salditt, T., "Pump-probe x-ray holographic imaging of laser-induced cavitation bubbles with femtosecond fel pulses," *Nature Communications* **12**(1), 3468 (2021).

[8] Hagemann, J., Vassholz, M., Hoeppe, H., Osterhoff, M., Rosselló, J. M., Mettin, R., Seiboth, F., Schropp, A., Möller, J., Hallmann, J., Kim, C., Scholz, M., Boesenberg, U., Schaffer, R., Zozulya, A., Lu, W., Shayduk, R., Madsen, A., Schroer, C. G., and Salditt, T., "Single-pulse phase-contrast imaging at free-electron lasers in the hard X-ray regime," *Journal of Synchrotron Radiation* **28**, 52–63 (Jan 2021).

[9] Ossig, C., Pyrlik, N., Carron, R., Fevola, G., Patjens, S., Strelow, C., Flügge, J., Kolditz, A., Siebels, J., Garrevoet, J., Spiers, K., Seyrich, M., Brückner, D., Hagemann, J., Seiboth, F., Schropp, A., Falkenberg, G., Mews, A., Schroer, C. G., Kipp, T., and Stuckelberger, M. E., "X-ray vision of cu(in,ga)se$_2$: from the ga/in ratio to solar-cell performance," *Journal of Physics: Energy* **4**, 045007 (oct 2022).

[10] Glazyrin, K., Khandarkhaeva, S., Fedotenko, T., Dong, W., Laniel, D., Seiboth, F., Schropp, A., Garrevoet, J., Brückner, D., Falkenberg, G., Kubec, A., David, C., Wendt, M., Wenz, S., Dubrovinsky, L., Dubrovinskaia, N., and Liermann, H.-P., "Sub-micrometer focusing setup for high-pressure crystallography at the Extreme Conditions beamline at PETRA III," *Journal of Synchrotron Radiation* **29** (apr 2022).

[11] Fevola, G., Ossig, C., Verezhak, M., Garrevoet, J., Guthrey, H. L., Seyrich, M., Brückner, D., Hagemann, J., Seiboth, F., Schropp, A., Falkenberg, G., Jørgensen, P. S., Slyamov, A., Balogh, Z. I., Strelow, C., Kipp, T., Mews, A., Schroer, C. G., Nishiwaki, S., Carron, R., Andreasen, J. W., and Stuckelberger, M. E., "3d and multimodal x-ray microscopy reveals the impact of voids in cigs solar cells," *Advanced Science* (Nov. 2023).

[12] Taylor, Z., Reddy, T., Fang, L., Oppermann, P., Kramer, P. L., Decker, F.-J., Seaberg, M., Chollet, M., van Driel, T., Halavanau, A., Hart, P., Dayton, M., Seiboth, F., Wang, W., Gee, C., Wilson, A., Margraf-O'Neal, R., Chatterjee, G., Chen, Y., Molesky, I. J., Wang, Y., Irvine, S., Stanton, J., Melendrez, C., Banta, K., Nelson, S., Thampy, V., Katagiri, K., Haubro, M., Liu, S., Pal, D., Moghimi, L., Tassone, C., and Dresselhaus-Marais, L., "High-resolution *in situ* characterization of laser powder bed fusion via transmission X-ray microscopy at X-ray free-electron lasers," *Journal of Synchrotron Radiation* **32** (May 2025).

[13] Wang, W., Döhrmann, R., Botta, S., Madsen, A., Schroer, C. G., and Seiboth, F., "Diamond x-ray lens cubes with integrated aberration compensation," *Optics Express* **33**, 22349 (May 2025).

[14] Shirk, M. D., Molian, P. A., and Malshe, A. P., "Ultrashort pulsed laser ablation of diamond," *Journal of Laser Applications* **10**(2), 64–70 (1998).

[15] Seiboth, F., "Refractive phase plates for aberration correction and wavefront engineering," *Synchrotron Radiation News* **35**, 43–48 (may 2022).

[16] Schropp, A., Boye, P., Feldkamp, J. M., Hoppe, R., Patommel, J., Samberg, D., Stephan, S., Giewekemeyer, K., Wilke, R. N., Salditt, T., Gulden, J., Mancuso, A. P., Vartanyants, I. A., Weckert, E., Schoder, S., Burghammer, M., and Schroer, C. G., "Hard x-ray nanobeam characterization by coherent diffraction microscopy," *Applied Physics Letters* **96**(9), 091102 (2010).

[17] Pfeiffer, F., "X-ray ptychography," *Nature Photonics* **12**(1), 9–17 (2018).

[18] Johnson, I., Bergamaschi, A., Billich, H., Cartier, S., Dinapoli, R., Greiffenberg, D., Guizar-Sicairos, M., Henrich, B., Jungmann, J., Mezza, D., Mozzanica, A., Schmitt, B., Shi, X., and Tinti, G., "Eiger: a single-photon counting x-ray detector," *Journal of Instrumentation* **9**(05), C05032 (2014).

[19] Seiboth, F., Wittwer, F., Scholz, M., Kahnt, M., Seyrich, M., Schropp, A., Wagner, U., Rau, C., Garrevoet, J., Falkenberg, G., and Schroer, C. G., "Nanofocusing with aberration-corrected rotationally parabolic refractive x-ray lenses," *Journal of Synchrotron Radiation* **25**, 108–115 (Jan 2018).

[20] Fienup, J. R., "Phase retrieval algorithms: a comparison," *Appl. Opt.* **21**, 2758–2769 (8 1982).

[21] Seiboth, F., Schropp, A., Scholz, M., Wittwer, F., Rödel, C., Wünsche, M., Ullsperger, T., Nolte, S., Rahomäki, J., Parfeniukas, K., Giakoumidis, S., Vogt, U., Wagner, U., Rau, C., Boesenberg, U., Garrevoet, J., Falkenberg, G., Galtier, E. C., Lee, H. J., Nagler, B., and Schroer, C. G., "Aberration correction for hard x-ray focusing at the nanoscale," *Proc. SPIE* **10386**, 103860A (2017).

[22] Schroer, C. G., Seiboth, F., Schropp, A., Achilles, S., Seyrich, M., Patjens, S., Stuckelberger, M. E., Garrevoet, J., Galbierz, V., Falkenberg, G., Kubec, A., David, C., Niese, S., and Gawlitza, P., "Hard x-ray wavefront engineering for aberration correction and beam shaping," in [*Advances in X-Ray/EUV Optics and Components XVII*], Mimura, H., Morawe, C., and Khounsary, A. M., eds., SPIE (oct 2022).